Available online at www.sciencedirect.com
SCIENCE DIRECT®
Journal of Sound and Vibration 290 (2006) 1175–1201
JOURNAL OF SOUND AND VIBRATION
www.elsevier.com/locate/jsvi

Analysis of the dispersion spectrum of fluid-loaded anisotropic plates: flexural-type branches and real-valued loops

A.L. Shuvalov*, O. Poncelet, M. Deschamps

Laboratoire de Mécanique Physique, Université Bordeaux 1, UMR CNRS 5469, 351, Cours de la Libération, F-33405 Talence Cedex, France

Received 1 June 2004; received in revised form 9 March 2005; accepted 12 May 2005
Available online 22 August 2005

Abstract

The subsonic spectrum of complex velocity versus real frequency in immersed anisotropic plates is considered for the various options of presupposed choice of modes in the loading fluid half-spaces. Two principal implications of the latter prerequisite are investigated. The first is related to the family of flexural-type branches (with origin at $v = 0$, $k = 0$), which evolve from the so-called A_0 and A_1 free-plate branches in a way that depends on the choice of fluid modes. By inspecting the low-frequency solutions of the dispersion equations corresponding to the different choices of fluid modes, a complete set of the flexural-type branches in an anisotropic fluid-loaded plate is identified. The result generalizes and also rectifies the interpretation commonly adopted for the isotropic case. The second issue is concerned with the real-valued loops on otherwise complex subsonic branches, involving the fluid mode increasing away from the plate. This phenomenon has been broadly discussed in numerical and experimental works on isotropic plates. The topological origin and shape of the real loops for an arbitrary plate can be readily viewed by way of the graphical layout of the sextic plate formalism. To this end, three possibilities are considered, namely, the sound velocity in the fluid, c_f, being (i) less than the Rayleigh velocity, (ii) greater than that but less than the bulk-wave threshold in the plate, and (iii) greater than the bulk-wave threshold. These lead to three basic configurations. In case (i), a closed real loop exists provided than the fluid-to-solid density ratio is smaller than a certain critical value, estimated here in a simple explicit form. Case (ii) is typically characterized by the presence of two open real-valued arches with common high-frequency limits. Case (iii) produces an infinite sequence of progressively narrowing real-valued arches, whose upper arms rise up to c_f and then transform into descending curves of solutions associated with the decreasing fluid modes (akin to

*Corresponding author. Fax: +33 5 40006964.
E-mail address: a.shuvalov@lmp.u-bordeaux1.fr (A.L. Shuvalov).

0022-460X/$ - see front matter
doi:10.1016/j.jsv.2005.05.015

the Sezawa continuum). A general overview of the locus of looping branches is supplied by analytical estimates and numerical examples.

1. Introduction

Ultrasonic inspection of fluid-loaded solid plates is one of the primary techniques of non-destructive testing and evaluation [1,2]. An immersed plate is insonified by means of concentrated-source loading or reflection/transmission, and information about its material characteristics is obtained by referring the acoustic response, one way or another, to the dispersion spectrum of plane guided waves (the plate eigenmodes). Knowledge of the spectrum properties is therefore essential for successful interpretation of the experimental data. In particular, the asymptotics for the fundamental branches in plates and beams have been broadly studied with regard to various applications in structural dynamics, see e.g. recent publications [3–6].

The dispersion spectrum of a lossless plate immersed in a non-viscous fluid may be represented in the form of real and complex branches of trace velocity $v(\omega)$ depending on real frequency. Taking ω as a real parameter fits with those experimental techniques in ultrasonics, in which the spatial rather than temporal aspect (see Refs. [7–9]) is most significant. The spectrum depends on the presupposed choice of the partial mode in the fluid half-spaces which may be taken as either decreasing or increasing into the fluid depth. Formally, boundary conditions on the plate–fluid interfaces may be posed for any fixed choice of the fluid mode, thus leading to different forms of the dispersion equation and ensuing velocity branches. For instance, the subsonic velocity range (i.e. below the speed of sound c_f in the loading fluid) contains the A and S real velocity branches, which correspond to the choice of decreasing fluid modes on both sides of the plate, and the A_0 complex velocity branch that involves increasing fluid modes. The (real part of) A_0 branch continues into the supersonic interval (above c_f), joining the continuum of complex branches of the leaky waves. It is evident, yet noteworthy, that the dispersion equation incorporating either both decreasing or both increasing fluid modes can yield a real velocity only below c_f but not above (apart from the locus of points $v > c_f$, at which the fluid plate are uncoupled), and that any one of these alternative choices may lead to real or complex subsonic velocity solutions.

The flexural-type A and A_0 branches, starting off at zero velocity and zero wavenumber, supersede the flexural branch $A_0^{(\mathrm{free})}$ of the unloaded (free) plate. This transformation, usually referred to as a split of $A_0^{(\mathrm{free})}$, is precipitated in the low-frequency vicinity of the origin branching point, where the fluid-loading effect is predominant. The intricacy of the onset of flexural-type branches was highlighted in the seminal paper on fluid-loaded isotropic plates by Osborne and Hart [10], which has underpinned the interpretation of an abundant numerical data accumulated since then. It is, however, notable that the low-frequency asymptotics attributed in Ref. [10] to the A and A_0 branches were derived from the same dispersion equation, although those branches imply different types of fluid mode. This leaves open a question as to how the choice of fluid modes is actually involved and should be handled in this instance. One more questioning point is that the theoretical framework established in Ref. [10] misses out another flexural-type branch, which evolves on fluid loading from the (pure imaginary) $A_1^{(\mathrm{free})}$ branch descending in the free plate from the first thickness resonance. In a broader perspective, the overall objective is to trace a

complete set of the flexural-type branches, arising in an arbitrary anisotropic immersed plate, taking into account the various choices of the fluid modes.

Another intriguing feature of the subsonic spectrum concerns the possibility of a real-valued loop on the A_0 branch. The closed loop for brass and aluminium plates under light-fluid loading, and its shrinking on increasing the density ratio value ρ_f/ρ, has been demonstrated numerically in Refs. [11,12]. This observation was used to suggest the reason why the same loop did not appear in the calculations, performed in Refs. [13–15] for isotropic plates immersed in water. Some useful data are presented in Ref. [16], where the arguments in favour of the loop existence and the criterion for this were sought by means of scrutinizing numerical results for various isotropic plate materials and loading fluids (all with c_f less than the Rayleigh velocity v_R in the plate). The debate on the accuracy of the implemented numerical routines (see Refs. [12,16,17]) has resolved at the conclusion that the A_0 real loop is certainly not an artefact. At the same time, an unequivocal explanation of its origin and explicit criterion for its occurrence in an arbitrary immersed isotropic plate (not to mention anisotropic ones) have not been established. This is certainly impossible within a pure numerical approach. In fact, the problem has been dealt with analytically in earlier papers on thin isotropic plates [18–20], where the pairwise real solutions $v_{A_0} < c_f$ ($< v_R$) were identified explicitly; however, an investigation of the locus of these roots and the existence considerations were beyond the scope of those papers. Developing an analytical description of the A_0 real loop in the $c_f < v_R$ setting, including the general case of anisotropic plates, is hoped to facilitate the challenging task of experimental observation of this loop; see Refs. [21,22].

The subsonic velocity spectrum undergoes some drastic changes when c_f exceeds the Rayleigh velocity v_R. Wave properties arising for various isotropic solids and loading fluids realizing the case $c_f > v_R$ have been studied recently [23–26]. A particularly striking feature, the arch of real A_0 velocities with a changeover point at $v_{A_0} = c_f$ to the branch of solutions involving the decreasing fluid modes, was observed numerically and experimentally for a water-loaded Plexiglas plate in Ref. [26]. This finding further motivates the search for a general understanding of the real-valued loops formation, one that would enable predictions of the looping branch occurrence and shape for arbitrary immersed plates. The problem certainly becomes much more involved in the case of anisotropic plate materials, but it turns out that there is a fundamental topological clue circumventing direct calculations.

The present paper aims to establish a clear picture of the family of flexural-type branches associated with various choices of the fluid modes, and of the real-valued loops occurring at $c_f < v_R$ and $v_R < c_f$, for the general case of fluid-loaded plates with unrestricted anisotropy. An efficient analytical tool for this is provided by the sextic plate formalism, developed in Refs. [27,28] and further elaborated in this paper. On this basis, the genesis of the flexural-type branches from the free-plate limit is traced, and their low-frequency onset is unravelled. The conditions underlying the existence of the real-valued loop on the A_0 branch at $c_f < v_R$ are revealed, and its parameters are quantified analytically in a simple explicit form. The locus of looping real-valued branches arising at $v_R < c_f$ is identified, and its invariant features for arbitrary anisotropic plates are established. The derivations are compared with the computer calculations performed for various materials. This paper is focused on the subsonic range of the dispersion spectrum, whereas the study of its supersonic domain is reserved for a companion paper [29].

2. Theoretical background

Consider an arbitrary anisotropic homogeneous lossless plate with a thickness $2h$, density ρ and elasticity tensor $\mathbf{c}$. Introduce the coordinate system $\{X, Y, Z\}$ with the axis Y along the unit normal $\mathbf{n}$ to the plate faces, and denote the unit vectors along X and Z by $\mathbf{m}$ and $\mathbf{t}$, respectively (Fig. 1). The aggregate displacement and traction for the packet of plane modes, propagating along the direction $\mathbf{m}\|X$ in the plate material, are assumed in the form

$$\begin{pmatrix} \mathbf{u} \\ \mathrm{i}k^{-1}\mathbf{n}\boldsymbol{\sigma} \end{pmatrix} = \boldsymbol{\xi}(y)\exp[\mathrm{i}k(x-vt)],\ \ \boldsymbol{\xi}(y) \equiv \begin{pmatrix} \mathbf{A}(y) \\ \mathbf{L}(y) \end{pmatrix}, \tag{1}$$

where k is the tangential wavenumber, $v = \omega/k$ is the trace velocity (which may be complex and hence different from the phase velocity), and $\omega = 2\pi f$ is the angular frequency. The Stroh formulation of the state-vector or sextic approach [30–33] incorporates the equation of motion and the stress–strain law into the first-order ordinary differential system

$$\mathrm{i}k\mathbf{N}(v)\boldsymbol{\xi}(y) = \frac{\mathrm{d}\boldsymbol{\xi}(y)}{\mathrm{d}y}, \tag{2}$$

with the 6×6 matrix

$$\mathbf{N}(v) = \begin{pmatrix} -(nn)^{-1}(nm) & -(nn)^{-1} \\ (mm) - (mn)(nn)^{-1}(nm) - \rho v^2\mathbf{I} & -(mn)(nn)^{-1} \end{pmatrix} \equiv \begin{pmatrix} \mathbf{N}_1 & \mathbf{N}_2 \\ \mathbf{N}_3 - \rho v^2\mathbf{I} & \mathbf{N}_1^{\mathrm{T}} \end{pmatrix}, \tag{3}$$

where T indicates the transpose, $\mathbf{I}$ is the identity matrix, and $(ab)_{jk} = a_i c_{ijkl} b_l$ for $\mathbf{a}$, $\mathbf{b} = \mathbf{m}$ or $\mathbf{n}$. The latter notation [31] allows writing the 3×3 contractions of c_{ijkl} and m_i, n_k in the basis $\{X_1, X_2, X_3\}$ of an arbitrary orientation with respect to the axes $\{X, Y, Z\} = \{\mathbf{m}, \mathbf{n}, \mathbf{t}\}$. By Eq. (2),

$$\boldsymbol{\xi}(h) = \mathbf{M}(h,-h)\boldsymbol{\xi}(-h),\ \ \mathbf{M}(h,-h) = \exp[2\mathrm{i}kh\mathbf{N}(v)] \equiv \begin{pmatrix} \mathbf{M}_1 & \mathbf{M}_2 \\ \mathbf{M}_3 & \mathbf{M}_1^{\mathrm{T}} \end{pmatrix}. \tag{4}$$

For future use, also introduce the admittance $\mathbf{Y}$:

$$\begin{pmatrix} \mathbf{A}(-h) \\ \mathbf{A}(h) \end{pmatrix} = \mathrm{i}\mathbf{Y}\begin{pmatrix} \mathbf{L}(-h) \\ -\mathbf{L}(h) \end{pmatrix}, \quad \mathbf{Y} = -\mathrm{i}\begin{pmatrix} -\mathbf{M}_3^{-1}\mathbf{M}_1^{\mathrm{T}} & -\mathbf{M}_3^{-1} \\ \mathbf{M}_2 - \mathbf{M}_1\mathbf{M}_3^{-1}\mathbf{M}_1^{\mathrm{T}} & -\mathbf{M}_1\mathbf{M}_3^{-1} \end{pmatrix}, \tag{5}$$

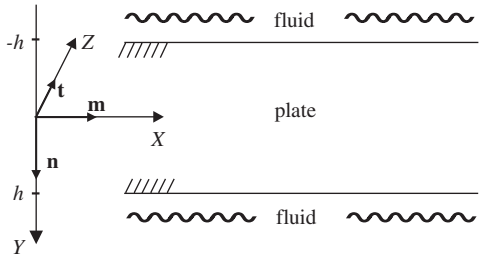

Fig. 1. The geometry of the problem.

which for real v, k is a Hermitian matrix [27]. In the present study, v and k may be complex: $v = v' + \mathrm{i}v''$, $k = k' + \mathrm{i}k''$, whereas ω is set to be real (and positive). For the latter reason, it is suitable to refer henceforth to the (v, ω)-parametrization (rather than (v, k), as in Refs. [27,28]).

Let the plate be immersed in a non-viscous compressible fluid with density ρ_f and speed of sound c_f. Partial modes propagating in the upper and lower fluid half-spaces $f1$ and $f2$, respectively, are taken in the form

$$\mathbf{u}_{f\alpha} = C_{f\alpha}(\mathbf{m} + p_{f\alpha}\mathbf{n}) \exp[\mathrm{i}k(x + p_{f\alpha}y - vt)], \quad \alpha = 1, 2, \tag{6}$$

where $C_{f\alpha}$ are scalar amplitudes and $p_{f\alpha}^2(v) = v^2/c_f^2 - 1$. Each parameter $p_{f\alpha}$ ($\alpha = 1, 2$) lies on one of the two Riemann sheets $n = 1, 2$ of the square root

$$S^{(n)}(v) = \sqrt{(v^2/c_f^2 - 1)\mathrm{e}^{\mathrm{i}2\pi(n-1)}}. \tag{7}$$

Let the argument of $v^2/c_f^2 - 1$ vary from 0 to 2π, i.e. the cut separating these sheets is defined by the equation $\operatorname{Im}\sqrt{v^2/c_f^2 - 1} = 0$, so that $\operatorname{Im} S^{(1)} > 0$, $\operatorname{Im} S^{(2)} < 0$. The properties of a fluid mode with its parameter $p_{f\alpha}$ taken on one or the other Riemann sheet are elucidated in Table 1. There, the mode type is characterized by the orientation of its wave vector $\mathbf{k}_{f\alpha} = k(\mathbf{m} + p_{f\alpha}\mathbf{n}) = \mathbf{k}' + \mathrm{i}\mathbf{k}''$, where $\mathbf{k}'$ is parallel to the energy flux and the sign of $\mathbf{k}'' \cdot \mathbf{n}$ determines increasing/decreasing into the fluid depth. Thus, prescribing either decreasing or increasing modes into the fluid on both sides of the plate ('symmetric choice', $p_{f1} = -p_{f2}$) leads, respectively, to

$$p_{f1} = (\operatorname{sgn} v')S^{(2)} = -p_{f2} = -(\operatorname{sgn} v')S^{(1)}, \tag{8}$$

or to

$$p_{f1} = (\operatorname{sgn} v')S^{(1)} = -p_{f2} = -(\operatorname{sgn} v')S^{(2)}, \tag{9}$$

where $\operatorname{sgn} v' = \pm 1$ at $v' \gtrless 0$. It is noted that the decreasing and increasing modes cannot be adequately distinguished in general by relating the modes merely to the sign of $\sqrt{v^2/c_f^2 - 1}$.

Proceeding from the standard boundary conditions at the plates–fluid interface, the dispersion equation can be expressed in the form

$$\left[Y_1^{(\mathbf{n})} - \frac{\mathrm{i}p_{f1}}{\rho_f v^2}\right]\left[Y_1^{(\mathbf{n})} + \frac{\mathrm{i}p_{f2}}{\rho_f v^2}\right] = Y_2^{(\mathbf{n})} Y_2^{(\mathbf{n})*}, \tag{10}$$

where

$$Y_1^{(\mathbf{n})} = \mathrm{i}\mathbf{n}\cdot\mathbf{M}_3^{-1}\mathbf{M}_1^{\mathrm{T}}\mathbf{n}, \quad Y_2^{(\mathbf{n})} = \mathrm{i}\mathbf{n}\cdot\mathbf{M}_3^{-1}\mathbf{n} \tag{11}$$

(see Eq. (5)), and * means complex conjugation of the function $Y_2^{(\mathbf{n})}$ but not of its arguments (if, say, $Y_2^{(\mathbf{n})} = Y_2^{(\mathbf{n})}(v, k)$, then $Y_2^{(\mathbf{n})*} \equiv Y_2^{(\mathbf{n})*}(v, k) \neq Y_2^{(\mathbf{n})*}(v^*, k^*)$ and $Y_2^{(\mathbf{n})} Y_2^{(\mathbf{n})*} \neq |Y_2^{(\mathbf{n})}|^2$ for complex v, k). The derivation of Eq. (10) is the same as in Ref. [28], except that now v, k may be complex and the choice of modes is not yet fixed. By Eqs. (8) and (9), taking either the decreasing or

Table 1
Correspondence between the type of the fluid mode (6) at real ω and the affiliation of its y-dependence parameter $p_{f\alpha}$ to one of the Riemann sheets of the square root $S^{(n)}$ (7) with the cut such that $\mathrm{Im}S^{(1)}>0$, $\mathrm{Im}S^{(2)}<0$. With reference to Fig. 1, the symbol | \ in the last column implies decreasing mode for fluid 1 and increasing mode for fluid 2; the symbol | / implies increasing mode for fluid 1 and decreasing mode for fluid 2

$p_{f\alpha}=S^{(1)}\quad (p''_{f\alpha}>0)$			
sign v'	sign v''	$\boldsymbol{k}'$ (solid), $\boldsymbol{k}''$ (dashed)	Mode type
>0	(1) >0		
	(2) <0		
<0	(3) >0		
	(4) <0		
$p_{f\alpha}=S^{(2)}\quad (p''_{f\alpha}<0)$			
>0	(5) >0		
	(6) <0		
<0	(7) >0		
	(8) <0		

Note: The values $S^{(1,2)}$in the limit $v''\to 0$:

$$v''\to -0:\ S^{(1)}=\begin{cases}-\sqrt{v'^2/c_f^2-1}+\mathrm{i}0, v'>c_f\\ \mathrm{i}\sqrt{v'^2/c_f^2-1}+\mathrm{i}0,\ |v'|<c_f;\\ \sqrt{v'^2/c_f^2-1}+\mathrm{i}0,\ v'<-c_f\end{cases}\quad v''\to +0:\quad S^{(1)}=\begin{cases}\sqrt{v'^2/c_f^2-1}+\mathrm{i}0, v'>c_f\\ \mathrm{i}\sqrt{v'^2/c_f^2-1}+\mathrm{i}0,\ |v'|<c_f\\ -\sqrt{v'^2/c_f^2-1}+\mathrm{i}0,\ v'<-c_f\end{cases}$$

$$S^{(2)}=-S^{(1)}.$$

increasing modes into the fluid on both sides specifies Eq. (10), respectively, as

$$\left[Y_1^{(\mathbf{n})}+\sqrt{Y_2^{(\mathbf{n})}Y_2^{(\mathbf{n})*}}-(\operatorname{sgn}v')Y_f\right]\left[Y_1^{(\mathbf{n})}-\sqrt{Y_2^{(\mathbf{n})}Y_2^{(\mathbf{n})*}}-(\operatorname{sgn}v')Y_f\right]=0, \tag{12}$$

or

$$\left[Y_1^{(\mathbf{n})}+\sqrt{Y_2^{(\mathbf{n})}Y_2^{(\mathbf{n})*}}+(\operatorname{sgn}v')Y_f\right]\left[Y_1^{(\mathbf{n})}-\sqrt{Y_2^{(\mathbf{n})}Y_2^{(\mathbf{n})*}}+(\operatorname{sgn}v')Y_f\right]=0, \tag{13}$$

with the fluid admittance

$$Y_f=-\frac{\mathrm{i}S^{(1)}}{\rho_f v^2}, \tag{14}$$

where $S^{(1)}$ stands for the value of the square root $\sqrt{v^2/c_f^2-1}$ taken in the first of the above-defined Riemann sheets. A reference to the sign of v' is essential for sorting out the flexural-type solutions near the branching point $v=0$. This implication apart, it is natural indeed to fix $v'>0$. For real $v<c_f$, in particular, $Y_f(v)$ by Eq. (14) is

$$Y_f=\frac{\sqrt{1-v^2/c_f^2}}{\rho_f v^2}. \tag{15}$$

Note that the factorized form of Eqs. (12) and (13), valid for arbitrary anisotropy of the plate, should not be mistaken for the factorization into equations for symmetric and antisymmetric branches in the presence of a symmetry plane parallel to the plate faces (see Ref. [1]; a link to the latter setting is discussed in Ref. [28]). In the case of a plate which is fluid-loaded on one side while free of traction on the other, the dispersion equations (12) and (13) simplify to the form $Y_1^{(\mathbf{n})}\mp(\operatorname{sgn}v')Y_f=0$.

A remaining possibility is to choose the increasing fluid mode on one side of the plate and the decreasing mode on the other side ('antisymmetric choice', $p_{f1}=p_{f2}$). In this case the dispersion equation (10) specifies

$$\left[Y_1^{(\mathbf{n})}+\sqrt{Y_2^{(\mathbf{n})}Y_2^{(\mathbf{n})*}}\right]\left[Y_1^{(\mathbf{n})}-\sqrt{Y_2^{(\mathbf{n})}Y_2^{(\mathbf{n})*}}\right]-Y_f^2=0, \tag{16}$$

where Y_f may be associated with any one of the Riemann sheets $S^{(1,2)}$. This is because the two options implied by the antisymmetric choice are indeed interchangeable as long as the fluid is the same on both sides of the plate. The modes in the upper and lower fluid half-spaces correspond to the same partial mode (any of the twos) in the infinite fluid, and it is therefore clear that Eq. (16) coincides with the condition of zero reflection (for inhomogeneous waves, if $v<c_f$).

The advantage of expressing the problem through the sextic plate formalism is that it endows the 'plate terms' of the dispersion equation with some significant analytical properties. We shall briefly summarize those that are relevant to the present study (omitting certain peculiarities). Denote by $\hat{v}_j(\omega)$ the (real) velocity branches $j=1,2,\ldots$ for the traction-free plate ($\mathbf{L}(\pm h)=\mathbf{0}$), which are defined by the dispersion equation $\det\mathbf{M}_3=0$. By Eq. (11), $Y_1^{(\mathbf{n})}(v,\omega)$ and $Y_2^{(\mathbf{n})}(v,\omega)$ diverge along $\hat{v}_j(\omega)$ and, for any fixed ω, the poles $\hat{v}_j$ are of the first order except for the folding

points on $\hat{v}_j$ (zeros of the in-plane group velocity). For real v,ω, the function $Y_1^{(\mathbf{n})}(v,\omega)$ is strictly real-valued, and, by definition, so is $\sqrt{Y_2^{(\mathbf{n})}Y_2^{(\mathbf{n})*}}=|Y_2^{(\mathbf{n})}|$. The residues of (complex) $Y_2^{(\mathbf{n})}(v,\omega)$ at the poles $\hat{v}_j(\omega)$ differ from that of (real) $Y_1^{(\mathbf{n})}(v,\omega)$ only by a phase factor (of unit absolute value); therefore, one of the functions $Y_1^{(\mathbf{n})}\pm|Y_2^{(\mathbf{n})}|$ is singular at $\hat{v}_j(\omega)$, while the other is smooth. Moreover, $Y_1^{(\mathbf{n})}\pm|Y_2^{(\mathbf{n})}|$ are positive at $v=0$ and represent monotonically increasing functions of v in a cut by any fixed $k>0$. The latter property is no longer valid in the cuts by a fixed ω; however, the functions $Y_1^{(\mathbf{n})}\pm|Y_2^{(\mathbf{n})}|$ of $v\,(>0)$ still have positive residues at the poles $\hat{v}_j$, given that the in-plane group velocity at $\hat{v}_j$ is positive as it is presumed henceforth for subsonic $\hat{v}_j(\omega)<c_f$ (this aspect is to be developed in Ref. [29]). It is also noted that, with ω being fixed, the values $Y_1^{(\mathbf{n})}\pm|Y_2^{(\mathbf{n})}|$ change sign on inverting sign of v (in no contradiction with their positiveness at $v=+0$, for, k changes from $+\infty$ to $-\infty$ on v passing zero), thus confirming sign invariance of the velocity solutions of Eqs. (12), (13) and (16). For $\omega\to\infty$ and the velocity below the plate's bulk-wave threshold, both functions $Y_1^{(\mathbf{n})}\pm|Y_2^{(\mathbf{n})}|$ tend exponentially fast to the same limit, which is the Lothe–Barnett normal admittance (inverse impedance) of the solid half-space $Y_\infty^{(\mathbf{n})}(v)$, monotonically increasing and having a pole at v_R [31,34].

Knowledge of these topologically invariant features of the 'plate terms' of the dispersion equation allows a transparent graphical way to pinpoint its real solutions at an arbitrary fixed ω (or k) and thereby to envisage corresponding real velocity branches. Let us exemplify how it works for identifying the real A and S subsonic velocity branches, involving the decreasing fluid modes. By Eq. (12) referred to real $v>0$, the sought branches are the intersections of the (v,ω) - parametrized surfaces $Y_1^{(\mathbf{n})}\pm|Y_2^{(\mathbf{n})}|$ with Y_f given by Eq. (15). A cut by a fixed ω, taken to be low (to add analytical estimates), is drawn in Fig. 2. It shows two topologically 'pinned' crossings, which are the points on the A and S branches for a given ω. Similar cuts by growing ω indeed

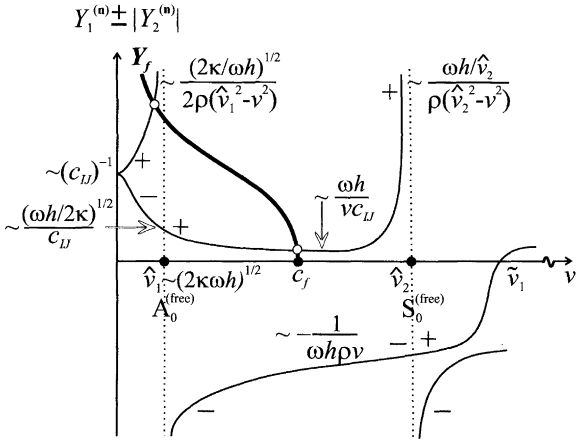

Fig. 2. A juxtaposition of the curves $Y_1^{(\mathbf{n})}\pm|Y_2^{(\mathbf{n})}|$ (thin line) and Y_f (bold line) as functions of real v at a fixed low ω ($\sqrt{2\kappa\omega h}\ll 1$, see Eq. (19)). The sign beside a 'plate' curve indicates the sign in its definition; c_{IJ} signifies certain combinations of elasticity coefficients (unspecified for brevity), and scale is not observed. The intersection points of the curves correspond to the A and S velocity solutions at a given ω.

contain the same fluid curve $Y_f(v)$, whereas the curves $Y_1^{(\mathbf{n})} \pm |Y_2^{(\mathbf{n})}|$ in each next cut come closer to one another within the velocity interval below the plate's bulk-wave threshold, and simultaneously the poles $\hat{v}_{1,2}(\omega)$ (points on the free-plate branches $A_0^{(\mathrm{free})}$, $S_0^{(\mathrm{free})}$) approach v_R. The limiting configuration in the cut by $\omega \to \infty$ evolves into the pattern with $Y_f(v)$ and the normal admittance $Y_\infty^{(\mathbf{n})}(v)$ of the half-space, which has been utilized in Ref. [34] to visualize the Scholte interfacial-wave velocity v_{Sch}. In view of these successive 'snapshots', it is immediate to figure out the entity of the A and$S$ branches and identify some fundamental properties invariant to the plate anisotropy, e.g., that the full stretch of the A and S branches must be bounded from above by the $A_0^{(\mathrm{free})}$ and $S_0^{(\mathrm{free})}$ branches, respectively. A similar approach will prove useful for identifying the loops of real-valued solutions related to the choice of increasing fluid modes. The complex-valued solutions cannot be spotted as easily; however, their approximate analytical estimates are also substantially facilitated by the outlined sextic plate formalism.

Unless otherwise specified, the forthcoming considerations are concerned with the general case of arbitrary plate anisotropy. In particular, there is no assumption of a symmetry plane parallel to the plate surfaces which leads to factorization of the dispersion equation into two for symmetric and antisymmetric branches. It is, however, convenient to retain the conventional A and S labelling of the branches, as long as it does not create ambiguity. These notations are going to be used on an equal footing with $v_j(\omega)$. It is recalled that the velocities for a free plate are labelled by a hat, i.e. $\hat{v}_j(\omega)$. Note also that the SH (shear horizontal) non-dispersive branch, which comes about in both free-plate and immersed-plate spectra when the sagittal plane $(\mathbf{m}, \mathbf{n})$ coincides with a symmetry plane of the plate, is not a pole for the functions $Y_{1,2}^{(\mathbf{n})}$ and thus does not show up on their graphical display. In this case, the notation $\hat{v}_2(\omega)$ (or $S_0^{(\mathrm{free})}$) will be assigned to the upper, dispersive fundamental branch; whereas in the absence of SH-uncoupling, when both upper fundamental branches in the free plate are dispersive, the notation $\hat{v}_2(\omega)$ implies the lower of the branches, while $\hat{v}_3(\omega)$ is reserved for the upper one.

3. The nomenclature and low-frequency onset of the flexural-type family

3.1. The flexural-type branches for the symmetric choice of fluid modes

This section is concerned with the velocity branches, which originate at $v = 0, k = 0$ (hence, $\omega = 0$) and in this sense are referred to as the flexural-type ones. It is noted that this definition excludes the branches with $k \neq 0$ at $\omega = 0$, $v = 0$. As everywhere else in this paper, ω is assumed to be real and therefore (v, ω)-parametrization is engaged. For future use, introduce coefficient

$$\kappa^2 = \frac{1}{12\rho}\mathbf{m} \cdot \mathbf{N}_3\mathbf{m} > 0, \tag{17}$$

which determines the low-frequency asymptotics

$$\hat{v}_1(\omega) = \sqrt{2\kappa\omega h} \tag{18}$$

of the $A_0^{(\mathrm{free})}$ flexural branch in an arbitrary anisotropic free plate (see Ref.[27]). For example, by Eqs. (17) and (3),

$$\kappa^2 = \frac{c_{11} - c_{12}^2/c_{22}}{12\rho}, \tag{19}$$

when the plate faces are parallel to a symmetry plane (c_{IJ} in Eq. (19) are referred to the coordinate axes X_1, X_2, X_3 taken along **m**, **n**, **t**, respectively). If in addition the sagittal plane (**m**, **n**) is also parallel to a symmetry plane, then $\sqrt{12}\kappa$ is the velocity $\hat{v}_2^{(0)}$ of the $S_0^{(\mathrm{free})}$ wave at $\omega = 0$.

Consider two different forms (12) and (13) of the dispersion equation, which are associated with alternative options of the symmetric choice of fluid modes. The low-frequency approximation for the onset of the flexural-type branches may be written as

$$\frac{\rho_f}{\rho} v^5 + \omega h v^4 - 4\kappa^2 (\omega h)^3 = 0, \tag{20}$$

$$-\frac{\rho_f}{\rho} v^5 + \omega h v^4 - 4\kappa^2 (\omega h)^3 = 0, \tag{21}$$

with the following correspondence:

$$(12) \Rightarrow (20) \text{ if } v' > 0, \ (21) \text{ if } v' < 0, \tag{22}$$

$$(13) \Rightarrow (20) \text{ if } v' < 0, \ (21) \text{ if } v' > 0. \tag{23}$$

Note that merely linking the sign in front of the 'fluid term' in Eqs. (20) and (21) with the choice of either decreasing or increasing modes would be incorrect—in fact, each of these equations describe one of the choices for the forward-propagating waves and the opposite choice for the backward-propagating waves.

Provided that the frequency is low enough to satisfy

$$\sqrt{\frac{\omega h}{2\kappa}} \ll \frac{\rho_f}{\rho}, \tag{24}$$

the roots of Eqs. (20) and (21) are approximated, respectively, in the form

$$(20) \Rightarrow v = \left[\frac{4\kappa^2(\omega h)^3}{\rho_f/\rho}\right]^{1/5} \exp\left(\mathrm{i}\frac{2\pi n}{5}\right) - \frac{1}{5}\frac{\omega h}{\rho_f/\rho}, \tag{25}$$

$$(21) \Rightarrow v = \left[\frac{4\kappa^2(\omega h)^3}{\rho_f/\rho}\right]^{1/5} \exp\left[\mathrm{i}\left(\frac{\pi}{5} + \frac{2\pi n}{5}\right)\right] + \frac{1}{5}\frac{\omega h}{\rho_f/\rho}, \tag{26}$$

where $n = 0, 1, \ldots, 4$ (Fig. 3). These two sets of roots are to be subjected to the conditions (22) and (23) in order to partition them into the solutions of the dispersion Eqs. (12) and (13).

Consider the choice of *decreasing* fluid modes leading to Eq. (12). Applying Eq. (22) to Eqs. (25) and (26) selects three pairs of roots,

$$v = \pm\left\{\left[\frac{4\kappa^2(\omega h)^3}{\rho_f/\rho}\right]^{1/5} \exp\left(\frac{\mathrm{i}\pi n}{5}\right) - \frac{1}{5}\frac{\omega h}{\rho_f/\rho}, \quad n = 0, -2, 2\right\} \Rightarrow \pm\{A, A_1, A_1^*\}, \tag{27}$$

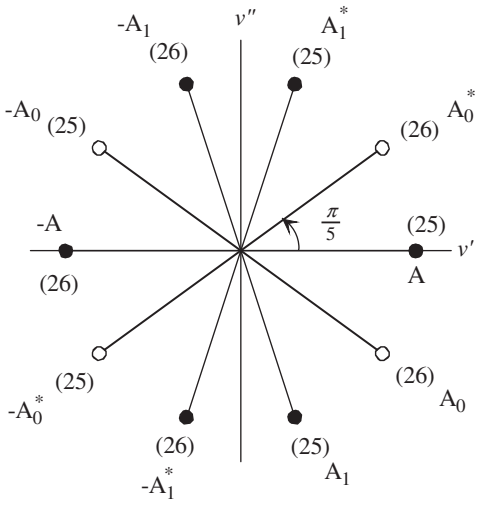

Fig. 3. The set of roots (25) and (26) in the complex v-plane and their correspondence to the solutions, presuming the choice of either decreasing (filled discs) or increasing (blank discs) modes in the fluids. For transparency, all the roots are placed on a circle by disregarding the small terms $\pm\frac{1}{5}\frac{\omega h}{\rho_f/\rho}$ in Eqs. (25) and (26).

where $\pm$ signs account for propagation in the opposite directions $\mathbf{m}$ and $-\mathbf{m}$; for definiteness, we are further referring only to the waves propagating along $\mathbf{m}$ ($v'>0$, see Fig. 3). Evidently, the real root with $n=0$ defines the onset $v_A(\omega)$ of the A branch. Two other complex-conjugated solutions, following from Eq. (27) at $n=\mp 2$, describe the onset of the A_1 and A_1^* branches, which evolve from the pure imaginary $A_1^{(\mathrm{free})}$ and $A_1^{(\mathrm{free})*}$ branches of the free plate. The notations may be specified by attributing A_1, say, to the velocity with a negative imaginary part. Thus, the A_1 wave ($n=-2$, $v''_{A_1}<0$) decays along $\mathbf{m}$ and involves the decreasing fluid modes, which carry the energy towards the plate (Table 1, the lines 6, 2 for $f1, f2$), whereas the A_1^* wave ($n=2$, $v''_{A_1^*}>0$) grows along $\mathbf{m}$ and includes the decreasing fluid modes with the energy flux directed away from the plate (see Table 1, the lines 5, 1 for $f1, f2$). In the typical case of small ρ_f/ρ, obviously, the absolute value of the imaginary part $v''_{A_1}(\omega)$ increases smoothly, whereas the real part $v'_{A_1}(\omega)$ with growing frequency first remains small in the measure of ρ_f/ρ and then soars up when ω gets close (also in the measure of ρ_f/ρ) to the cutoff value.

Now let us deal with the choice of *increasing* fluid modes described by Eq. (13). Condition (23) picks two remaining pairs of roots from Eqs. (25) and (26), namely,

$$v=\pm\left\{\left[\frac{4\kappa^2(\omega h)^3}{\rho_f/\rho}\right]^{1/5}\exp\left(\frac{\mathrm{i}\pi n}{5}\right)+\frac{1}{5}\frac{\omega h}{\rho_f/\rho},\quad n=-1,\,1\right\}\Rightarrow\pm\{A_0,\,A_0^*\},\tag{28}$$

see Fig. 3. The A_0 wave ($n=-1$, $v''_{A_0}<0$) decays along $\mathbf{m}$ and includes the increasing fluid modes outflowing from the plate (Table 1, lines 2, 6 for $f1, f2$), whereas its complex-conjugate A_0^* ($n=1$) grows along $\mathbf{m}$ and involves the increasing fluid modes carrying energy towards the plate (see Table 1, lines 1, 5 for $f1, f2$). According to Eqs. (27) and (28), the real part $v'_{A_0}(\omega)$ for extremely small ω lies below the real-valued A and $A_0^{(\mathrm{free})}$ branches, but it certainly rises above these two very soon with growing frequency.

Compare the obtained solutions with the results inferred for the A and A_0 branches in an isotropic plate by Osborne and Hart [10]. The isotropic version of the leading term for the A branch (Eq. (27) with $n = 0$) coincides with the formula given in [10]. However, the asymptotics assigned in Ref.[10] to the A_0 branch corresponds in fact to the A_1 branch (Eq. (27) with $n = -2$), whereas the actual A_0 asymptotics (Eq. (28) with $n = -1$) was missed. This oversight is due to the fact that both asymptotics in Ref.[10] were derived from the same dispersion equation related to the decreasing fluid modes.

For a numerical example we take an anisotropic plate represented by the $(1\bar{1}0)$ cut (**n** is parallel to $[1\bar{1}0]$) of cubic copper, choose the orientation [110] for the propagation direction **m**, and assume water ($\rho_f = 1\,\mathrm{g/cm^3}$, $c_f = 1.5\,\mathrm{mm/\mu s}$) as the loading fluid. The material parameters used for copper are as follows: $\rho = 8.932\,\mathrm{g/cm^3}$ and $c_{11} = c_{22} = 222$, $c_{33} = 170$, $c_{12} = 71$, $c_{13} = c_{23} = 123$, $c_{44} = c_{55} = 75.5$, $c_{66} = 23.5\,\mathrm{GPa}$ in the reference basis $\{X_1, X_2, X_3\} = \{\mathbf{m}, \mathbf{n}, \mathbf{t}\}$. The low-frequency onset of the flexural-type branches is compared with the analytical asymptotics in Fig. 4, and the full extent of the branches is shown in Fig. 5. It is pertinent to note that the chief purpose of the asymptotics (27) and (28) is an accurate account of the extreme low-frequency onset $\sqrt{\omega h/2\kappa} \ll \rho_f/\rho$ of the flexural branches, which decides their ramification. For a higher frequency, these asymptotics should be replaced by a more appropriate approximation. For instance, reasonable estimates for the A and A_1 branches in the range $\rho_f/\rho \ll \sqrt{\omega h/\kappa} \ll 1$ may be given

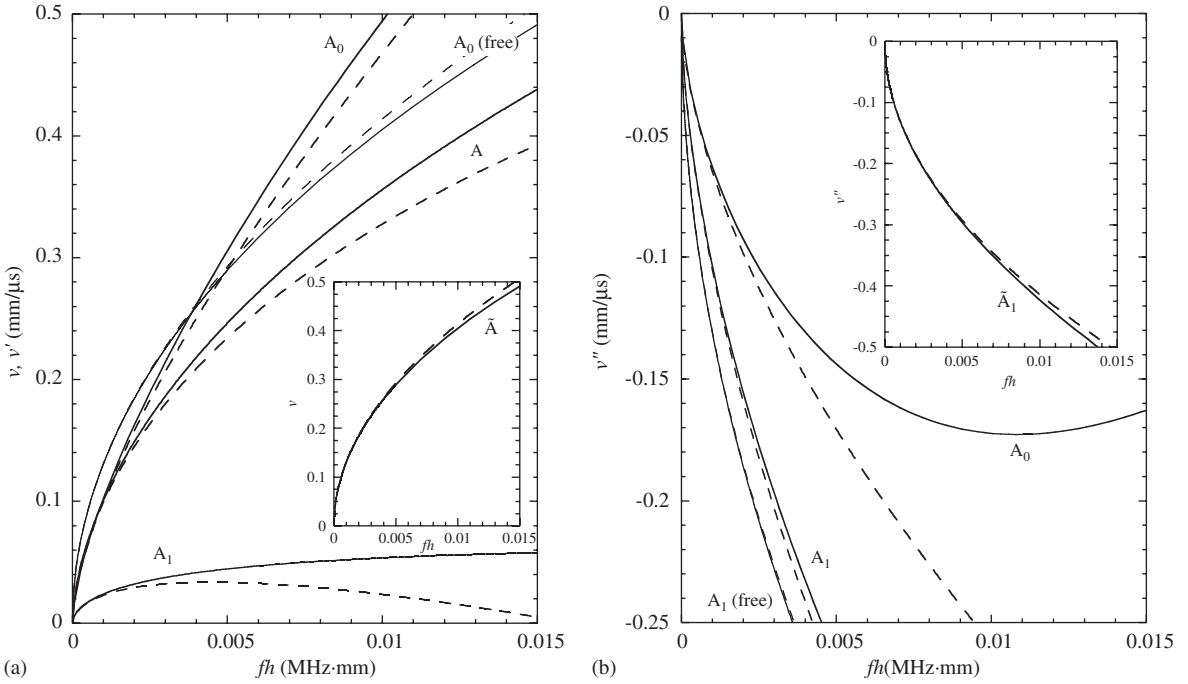

Fig. 4. The exact low-frequency onset (solid lines) and corresponding asymptotics (27), (28) and (30) (dashed lines) of the flexural-type branches, associated with various choices of the fluid modes, for the [110] propagation direction in the $(1\bar{1}0)$-cut copper plate immersed into water. For comparison, the flexural-type $A_0^{(\mathrm{free})}$, $A_1^{(\mathrm{free})}$ branches in the free plate are also displayed. (a) Real v and real parts $v' = \mathrm{Re}\,v$. (b) Imaginary parts $v'' = \mathrm{Im}\,v$. The $\tilde{A}$ and $\tilde{A}_1$ branches, which at low ω are very close to $A_0^{(\mathrm{free})}$ and $A_1^{(\mathrm{free})}$, are displayed separately in the insets.

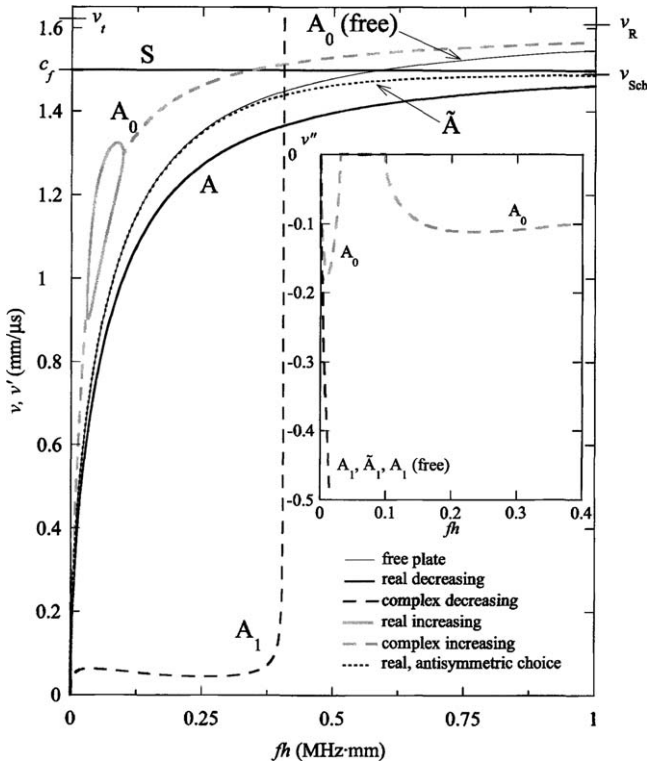

Fig. 5. The family of flexural-type branches, associated with various choices of the fluid modes, for the [110] propagation direction in the $(1\bar{1}0)$-cut copper plate immersed into water. The notations for different branches are explained on the plot. The S branch and the free-plate $A_0^{(\mathrm{free})}, A_1^{(\mathrm{free})}$ branches are added for comparison. The main plot shows real v and $v' = \mathrm{Re}\, v$; the inset displays $v'' = \mathrm{Im}\, v$.

by the relations

$$v_A(\omega) = \sqrt{2\kappa\omega h} - \frac{\rho_f \kappa}{2\rho}, \quad v_{A_1}(\omega) = \frac{\rho_f \kappa}{2\rho} - \mathrm{i}\sqrt{2\kappa\omega h}. \tag{29}$$

The development of the A_0 branch is complicated by the possible arrival of the real loop (see Fig. 5), which is dealt with in the next section.

Thus, the low-frequency asymptotics of the free-plate dispersion equation, which is of the fourth degree in v, transforms due to fluid loading into two different fifth degree equations (20) and (21). Correspondingly, the two pairs of the free-plate branches, $\pm\{A_0, A_1\}^{(\mathrm{free})}$, evolve into the five pairs for the immersed plate, $\pm\{A, A_1, A_1^*\}$ and $\pm\{A_0, A_0^*\}$, related to the choice of decreasing and increasing fluid modes, respectively. As it has been pointed out, the dispersion equation, associated with any one of the alternative choices, is a *combination* of Eqs. (20) and (21) for inverse propagation directions (not that one of these equations stands for one choice and the other equation stands for the other choice). This is why the distribution of the solutions between the two choice options is uneven. The $A_0^{(\mathrm{free})}$ branch transforms into the A or A_0 branch for the decreasing or increasing fluid modes, respectively, but the $A_1^{(\mathrm{free})}$ $(= -A_1^{(\mathrm{free})*})$ branch, tending towards the first thickness resonance, gives rise only to a single (complex) A_1 branch and for the

choice of, specifically, decreasing fluid modes. It is also noteworthy in this context that the often encountered reference to A and A_0 branches arrival as a split of $A_0^{(\mathrm{free})}$ is not perfectly accurate, for, it might be understood as if fluid loading perturbs a degenerate solution, which is certainly not the case—in fact, the $A_0^{(\mathrm{free})}$ branch transforms into either A or A_0 for different perturbations, described by two different forms of the dispersion equation.

3.2. The flexural-type branch for the antisymmetric choice of fluid modes

It is instructive to inspect the flexural-type solutions of the dispersion equation in form (16), which corresponds to the choice of the increasing mode on one side of the plate and the decreasing mode on the other (the antisymmetric choice). For such a setting, the pair of the free-plate branches $A_0^{(\mathrm{free})}$ and $A_1^{(\mathrm{free})}$ transforms into two branches remaining, respectively, real and pure imaginary. Denote them as $\tilde{A}$ and $\tilde{A}_1$. The real $\tilde{A}$ branch may be spotted by means of the graphical analysis of Eq. (16), similar to Fig. 2. It readily follows that the $\tilde{A}$ branch is very close from below to the $A_0^{(\mathrm{free})}$ branch for small ω, but then tends from above to the A branch, both having the same high-frequency limit v_{Sch}. The $\tilde{A}_1$ branch trails close to $A_1^{(\mathrm{free})}$. The low-frequency asymptotics for $\tilde{A}$ and $\tilde{A}_1$ branches are

$$v_{\tilde{A}} = \sqrt{2\kappa\omega h}\left[1 - \sigma\left(\frac{\rho_f}{\rho}\right)^2 \kappa\omega h\right], \quad v_{\tilde{A}_1} = \mathrm{i}\sqrt{2\kappa\omega h}\left[1 + \sigma\left(\frac{\rho_f}{\rho}\right)^2 \kappa\omega h\right], \tag{30}$$

where $\sigma = \rho\mathbf{n}\cdot(\mathbf{N}_1\mathbf{N}_3^{-1}\mathbf{N}_1^{\mathrm{T}} - \mathbf{N}_2)\mathbf{n}$; see Eq. (3). If, for instance, the plane of plate faces and the sagittal plane are both parallel to symmetry planes, then simply $\sigma^{-1} = 12\kappa^2 = \hat{v}_2^{(0)\,2}$ (see Eq. (19)). The $\tilde{A}$ and $\tilde{A}_1$ branches are also displayed in Figs. 4 and 5, along with the branches related to the symmetric choice of fluid modes. Note that the flexural-type branch with a real low-frequency onset has been obtained numerically in Refs. [15,35] for the antisymmetric choice of fluid modes applied to an isotropic plate in contact with two different fluids on the opposite sides.

4. The real-valued loop for the A_0 branch at $c_f < v_R$

The sextic plate formalism lends a graphical way to unambiguously identify the origin of the real-valued A_0 loop. The underlying considerations are the same as those expounded in Fig. 2 for the A and S branches. The only difference is that here we are concerned with the waves

Fig. 6. Graphical identification of the real-valued looping branches by spotting intersections (shaded circles) of the plate-admittance curve(s) as functions of v at a fixed ω (thin lines) and the curve $-Y_f(v)$ (bold line), associated with the choice of increasing fluid mode. Diagrams (a), (b) and (c_1), taken for successively growing values of ω, illustrate the origin and closure of the A_0 loop in the case $c_f < v_R$; diagram (c_2) demonstrates the presence of the A_0 and S_0 open arches for high ω in the case $v_R < c_f < v_t$ (positive curves in ($c_{1,2}$) are omitted). The arrows attached to the free-plate poles indicate their tendency with increasing ω. Diagrams (d) and (e), describing the case $v_t < c_f$, visualize the changeover of the upper arm of the arches (first one herein): the intersection point moves from $-Y_f(v)$ to $Y_f(v)$, the latter associated with the choice of decreasing fluid mode. No strict scale is observed, but the plots (d), (e) imply larger ρ_f/ρ than in (a)–(c_1). Diagrams (f) and (g) explain a specific shape of the first arch for the same plate but fluid-loaded on one side and free on the other at $v_R < c_f < v_t$ (f) and $v_t < c_f$ (g).

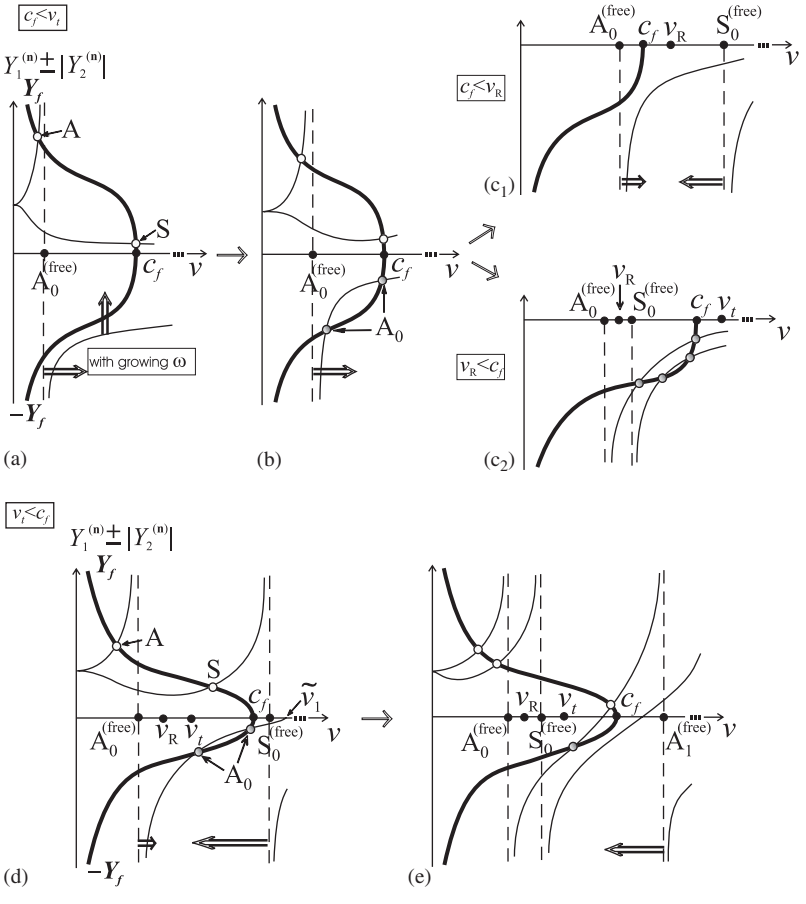

one-sided fluid loading

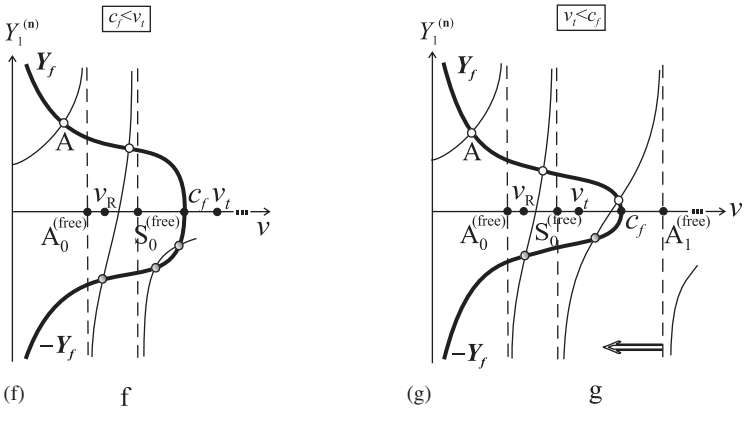

incorporating increasing fluid modes; hence, the dispersion equation is in form (13), and so it is now the curve $-Y_f(v)$, whose intersections with the 'plate curves' $Y_1^{(\mathbf{n})}(v) \pm |Y_2^{(\mathbf{n})}(v)|$ in constant-frequency cuts indicate the real velocity solutions sought. The evolution of events with growing ω is elucidated in Fig. 6a–c$_1$. For low frequency, the negative branch of $Y_1^{(\mathbf{n})} - |Y_2^{(\mathbf{n})}|$ on the right-hand side of the first free-plate pole $\hat{v}_1(\omega)$ (that is, $A_0^{(\mathrm{free})}$) is inversely proportional to ωh; hence, intersection with $-Y_f$ is impossible (Fig. 6a, $\sqrt{\omega h/2\kappa} \ll \rho_f/\rho$). So the low-frequency onset of the A_0 velocity branch is always complex, in accordance with Eq. (28). As frequency increases, the curve $Y_1^{(\mathbf{n})} - |Y_2^{(\mathbf{n})}|$ moves upwards and simultaneously to the right, pushed by the shifting $A_0^{(\mathrm{free})}$-pole. Therefore, at a certain frequency the curves $Y_1^{(\mathbf{n})} - |Y_2^{(\mathbf{n})}|$ and $-Y_f$ may touch each other (signifying confluence of the A_0 and A_0^* branches), and then, with further ω growth, intersect twice in between $\hat{v}_1(\omega)$ and c_f (Fig. 6b). The ratio of the plate and fluid admittances is proportional to ρ_f/ρ; hence, the contact of $Y_1^{(\mathbf{n})} - |Y_2^{(\mathbf{n})}|$ and $-Y_f$ curves is stipulated by the criterion that ρ_f/ρ is less than a certain critical value,

$$\rho_f/\rho \leqslant (\rho_f/\rho)_{\mathrm{crit}}. \tag{31}$$

Provided that c_f is smaller than the Rayleigh velocity v_R, the free-plate flexural pole keeps moving to the right with growing ω, so the two intersections merge into a tangency once more, and then the curves $Y_1^{(\mathbf{n})} - |Y_2^{(\mathbf{n})}|$ and $-Y_f$ move apart each other (Fig. 6c$_1$, $\sqrt{\omega h/2\kappa} \gg \rho_f/\rho$), meaning that the A_0 velocity branch becomes complex again before the $A_0^{(\mathrm{free})}$ branch crosses c_f.

Thus, loading any plate by a sufficiently light fluid with $c_f < v_R$ entails a real-valued A_0 subsonic loop, assuredly closed and bounded from below by the $A_0^{(\mathrm{free})}$ branch. Fig. 6 shows that for $\rho_f/\rho \ll 1$ the lower arm of the loop stretches alongside the $A_0^{(\mathrm{free})}$ branch, being above it in the measure of ρ_f/ρ, while the upper arm ascends rapidly at $\sqrt{\omega h/\kappa} \sim \rho_f/\rho$ and then remains below c_f, close to it in the measure of $(\rho_f/\rho)^2$. Increasing ρ_f/ρ causes the loop to shrink and eventually degenerate at a critical value $(\rho_f/\rho)_{\mathrm{crit}}$ into a point $(v, \omega)_{\mathrm{crit}}$. These observations are in agreement with the computer simulations for the brass and aluminium isotropic immersed plates performed in Refs.[11,12]. The graphical display of the sextic plate formalism provides a clear evidence of the basic trends of the A_0 loop for an arbitrary anisotropic plate material.

It is of principal interest to evaluate the A_0 real loop and particularly the condition for its existence. An exact and explicit analytical formulation is certainly beyond reach. However, noting that the loop is usually confined to the low-frequency domain enables approximate estimates. Assuming $\omega h/v \ll 1$ allows approximating the dispersion equation (13), squared to lift the radical $\sqrt{1 - v^2/c_f^2}$ (the latter is not replaced by 1, as opposed to Eqs. (20) and (21)), in the form of the fifth-order polynomial in v^2,

$$\begin{gathered}(r^2 + a)x^5 - ax^4 - 2ab^2x^3 + 2a^2bx^2 + a^3b^2x - a^3b^2 = 0,\\ x = v^2/c_f^2,\ r = \rho_f/\rho,\ a = (\omega h)^2/c_f^2,\ b = 4\kappa^2/c_f^2.\end{gathered} \tag{32}$$

Its two real roots, describing the pair of points on the upper and lower arms of the real velocity loop for given ω and ρ_f/ρ, may be roughly evaluated, with reference to

Eq. (18), as

$$(v_{A_0})_1^2 = 2\kappa\omega h\left(1+\frac{\rho_f}{\rho}\sqrt{\frac{2\kappa}{\omega h}}\right), \quad (v_{A_0})_2^2 = c_f^2\left[1-\left(\frac{\rho_f c_f}{\rho\omega h}\right)^2\right]. \tag{33}$$

The estimate for the frequency values at the left and the right extreme points of the loop may be suggested in the form

$$\omega^{(\mathrm{ex})}_{\mathrm{left,right}} = \frac{c_f^2}{4\kappa h}\left(1\mp\sqrt{1-4\sqrt{2}\frac{\rho_f}{\rho}\frac{\kappa}{c_f}}\right)^2, \tag{34}$$

whence follows the approximation for the critical density ratio, at which the loop closes up, and for the coordinates of the corresponding degeneracy point,

$$\left(\frac{\rho_f}{\rho}\right)_{\mathrm{crit}} = \frac{c_f}{4\sqrt{2}\kappa}, \tag{35a}$$

$$(v,\,\omega)_{\mathrm{crit}} = \left(\frac{c_f}{\sqrt{2}},\,\frac{c_f^2}{4\kappa h}\right). \tag{35b}$$

It is, however, noted that the foregoing estimates are stipulated by some compromising simplifications and are therefore fairly loose. A more stringent procedure for evaluating the critical parameters of the A_0 loop at its termination point implies, firstly, demanding a zero discriminant of Eq. (32), thereby eliminating x and arriving at the fifth-order polynomial in a that defines the frequency at the left and the right extreme points of the loop as a function of r and b, and, secondly, demanding a zero discriminant of the latter equation to obtain the critical density ratio, which is then inserted back into the discriminants to recover the critical frequency and velocity. Implementing this procedure with the aid of the symbolic-algebra package yields the relations

$$\left(\frac{\rho_f}{\rho}\right)_{\mathrm{crit}} = \frac{c_f}{6\sqrt{3}\kappa}, \tag{36a}$$

$$(v,\,\omega)_{\mathrm{crit}} = \left(\frac{c_f}{\sqrt{2}},\,\frac{c_f^2}{4\sqrt{3}\kappa h}\right), \tag{36b}$$

which still have a remarkably simple form. It admits an especially lucid representation in the case of an orthorhombic setting, when $\sqrt{12}\kappa = \hat{v}_2^{(0)}$, see Eq. (19).

Knowledge of the dependence of the critical density ratio $(\rho_f/\rho)_{\mathrm{crit}}$ on c_f is quite useful. Plotted in the plane $(\rho_f/\rho,\, c_f)$, this dependence identifies the domain $\rho_f/\rho<(\rho_f/\rho)_{\mathrm{crit}}$, $c_f<v_R$ of the A_0 real loop existence for a given plate on its loading by various fluids. Fig. 7 presents a comparison between the analytical approximations (35) and (36) of the critical parameters $(\rho_f/\rho)_{\mathrm{crit}}$, v_{crit}, $(fh)_{\mathrm{crit}}$ $(f=\omega/2\pi)$ versus c_f and their exact numerical evaluation for the case of [110] propagation direction in the $(1\bar{1}0)$-cut copper plate subjected to fluid loading. It is seen that the 'accurate low-frequency' estimate (36) is quite precise at relatively small c_f (when the loop terminates at low frequency), and that it only marginally deteriorates for c_f approaching v_{R}. Note that the exact

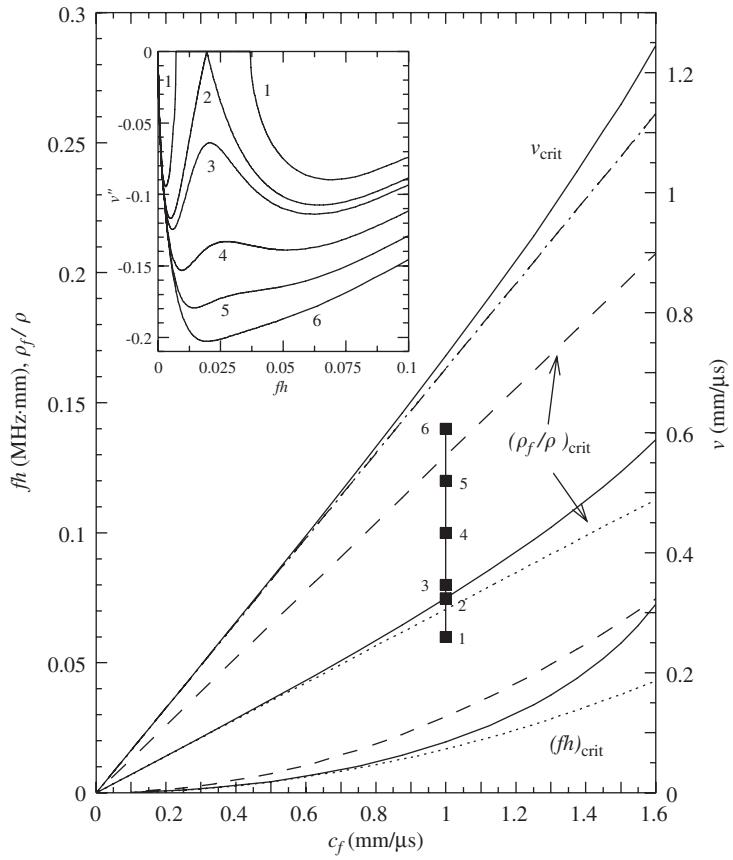

Fig. 7. Critical parameters, corresponding to the termination of the A_0 real loop, as a function of the speed of sound c_f in loading fluid for the [110] propagation direction in the immersed $(1\bar{1}0)$-cut copper plate. Solid lines are the exact numerical curves, dashed and dotted lines are approximations (35) and (36), respectively. The inset demonstrates 'the healing' of the dip on the attenuation curve once the loop disappears. It shows v''_{A_0} versus frequency at a fixed $c_f = 1$ mm/μs and the value ρ_f/ρ, which is less (curve 1), equal (curve 2) and greater (curves 3–6) than $(\rho_f/\rho)_{crit}$ (the probe values ρ_f/ρ are indicated by the correspondingly numbered squares on the straight line).

curves for $(\rho_f/\rho)_{crit}$ and $(fh)_{crit}$ appear to be bounded by Eq. (36) on one side and by the 'loose' estimate (35) on the other, for which reason the latter may also be helpful.

As regards application of estimate (36a) for verifying criterion (31) for the A_0-loop existence in plates of various materials, this may be demonstrated by appealing to the plate–fluid combinations, for which the absence or presence of the loop has been tested numerically in Ref.[16], see Table 3 there (note that its categorization of the air-loaded plates with an extremely small density ratio as not having the loop is indeed an oversight). In the cases of the loop existence (entries 1–6 tabulated in Ref.[16]), the actual value of ρ_f/ρ is below the critical threshold $(\rho_f/\rho)_{crit}$ approximated by Eq. (36a) except on one occasion (entry 1), for which the actual $\rho_f/\rho \approx 0.118$ is only fractionally greater than the critical value 0.114 given by Eq. (36a). Bearing in mind that the latter tends to slightly underestimate the exact $(\rho_f/\rho)_{crit}$ (the more so at higher c_f, see Fig. 7), the

loop presence for this entry may be said to be also predicted by Eq. (36a) with regard for the 'confidence interval'. For all the plate-fluid combinations used in Ref.[16] to exemplify the loop non-existence (entries 7–11), the actual value of ρ_f/ρ markedly exceeds the critical-threshold estimate (36a), thus endorsing its reliability.

The aforementioned examples from Ref.[16] are concerned with isotropic plates. It is therefore pertinent to point out that the approximate evaluation of the critical parameters of the A_0 loop is valid for an arbitrary anisotropic plate. The derivation reveals that the leading dependence of $(\rho_f/\rho)_{\text{crit}}$ on the plate material elastic properties is through a single parameter κ. Hence, the surface, defined in the 3D $(\rho_f/\rho, c_f, \kappa)$-space by the conjunction of Eq. (36a) and the inequality $c_f < v_R$, can serve as an approximate 'phase diagram' of the A_0 loop existence for arbitrary plates and loading fluids. The greater the c_f and the smaller the κ, the less accurate the low-frequency assumption implied on evaluating the loop termination by Eq. (36a), and hence the larger the error of approximation (underestimation) of the exact $(\rho_f/\rho)_{\text{crit}}$. Nevertheless, the derived analytical benchmark with its very simple explicit form appears worthwhile. Thus, with reference to the practically common case of water as a loading fluid, the loop existence may be expected for dense metal plates and also for 'slow directions' in comparatively soft fibre-composite plates (propagation across the fibres); whereas it is less likely for the latter type of plates when the propagation direction is 'fast' (along the fibres).

Note in conclusion that exactly the same existence considerations for the A_0 loop apply to the one-sided fluid loading, except that the estimate for $(\rho_f/\rho)_{\text{crit}}$ in this case is two times greater as compared to Eqs. (35a) and (36a).

5. The locus of real loops for $v_R < c_f$

If the Rayleigh velocity v_R is less than c_f, the subsonic velocity spectrum may acquire various types of real-valued looping branches. Two basically dissimilar patterns, that arise depending on whether $c_f\,(>v_R)$ is less or greater than the bulk-wave threshold in the plate, can be identified for an arbitrary anisotropic plate without any explicit calculations, resorting once again to the graphical display of the sextic plate formalism. To illuminate the principal idea, we will straighten its exposition by referring basically (unless otherwise indicated) to the case of SH-wave uncoupling. With a view to facilitate a link to the numerical diagrams for isotropic plates, the bulk-wave threshold, generally related to the in-plane or out-of-plane lateral wave, is represented below by the transverse-wave velocity v_t. Also, a typical situation is assumed when the least zero $\tilde{v}_1(\omega)$ of the curves $Y_1^{(\mathbf{n})} \pm |Y_2^{(\mathbf{n})}|$ remains greater than v_t at any high ω, so that their joint high-frequency limit taken at v_t is negative: $\left(Y_1^{(\mathbf{n})} \pm |Y_2^{(\mathbf{n})}|\right)_{v_t,\omega} \to Y_\infty^{(\mathbf{n})}(v_t) < 0$, thus barring the existence of the second subsonic Scholte wave [34,36].

5.1. The case $v_R < c_f < v_t$

Consider the choice of increasing fluid modes (Eq. (13)). The topology of the A_0 real loop origin in the case $v_R < c_f$ is basically the same as at $c_f < v_R$ (Fig. 6a,b). However, now the free-plate pole, corresponding to the $A_0^{(\text{free})}$ branch, remains 'under' the curve $-Y_f(v)$ at a high frequency anyhow.

As a consequence, given that the relative difference between c_f and v_R is not too small compared to ρ_f/ρ (see below), the pair of intersections of the plate and fluid curves persists up to $\omega \to \infty$ (Fig. 6c$_2$), meaning that the locus of A_0 real velocities forms an open arch lying above $A_0^{(\mathrm{free})}$. It may emerge at a markedly higher frequency than in the case $c_f < v_R$, and hence is allowed for ρ_f/ρ well exceeding the critical value $\left(\rho_f/\rho\right)_{\mathrm{crit}}$ conditioning the loop at $c_f < v_R$. Moreover, once the A_0 arch arises, then for higher ω the next curve $Y_1^{(\mathbf{n})} - |Y_2^{(\mathbf{n})}|$, dragged along by the pole $S_0^{(\mathrm{free})} \to v_R$, also comes to intersect with the curve $-Y_f(v)$ (Fig. 6c$_2$). Thus, the second arch of real solutions appears, lying strictly above the $S_0^{(\mathrm{free})}$ branch after the latter enters the subsonic interval. Evidently, this arch is not related to the flexural-type family. Provided ρ_f/ρ is small enough so that the real part of the S_0 leaky-wave velocity branch bends downwards alongside $S_0^{(\mathrm{free})}$, it is then this branch that coalesces with its complex conjugate to give rise to the second arch, which may be therefore labelled S_0.

Two 'plate curves', intersecting with $-Y_f(v)$ in Fig. 6c$_2$, tend exponentially to the same curve $Y_\infty^{(\mathbf{n})}(v)$ at $\omega \to \infty$ and $v \leqslant v_t$, so the lower arms of the two arches and their upper arms share the high-frequency limits $v_\infty^{(1)}$ and $v_\infty^{(2)}$, respectively, which are approximated for small enough ρ_f/ρ as

$$v_\infty^{(1)} = v_R\left(1 + \frac{\rho_f}{\rho}\frac{a_R}{2\sqrt{1 - v_{\mathrm{R}}^2/c_f^2}}\right), \quad v_\infty^{(2)} = c_f\left\{1 - \frac{1}{2}\rho_f^2\left[c_f^2\, Y_\infty^{(\mathbf{n})}(c_f)\right]^2\right\}, \tag{37}$$

with $a_R = -2\rho v_R\left[\mathrm{d}\left(1/Y_\infty^{(\mathbf{n})}\right)/\mathrm{d}v\right]_{v_R}^{-1}$. They describe the interfacial waves, that incorporate the modes decreasing into the solid half-space along with the mode increasing into the fluid (as opposed to the Scholte wave which involves the decreasing fluid mode). By Eq. (37), $v_\infty^{(1)}$ exceeds v_R in the measure of ρ_f/ρ, while $v_\infty^{(2)}$ is less than c_f in the measure of $(\rho_f/\rho)^2$. Evidently, the inequality

$$v_\infty^{(1)} < v_\infty^{(2)} \quad \left(\approx c_f \text{ at } \left(\rho_f/\rho\right)^2 \ll 1\right) \tag{38}$$

ensures the existence of the A_0 and S_0 open arches. This condition means that the relative distance between v_R and c_f ($< v_t$) must be large enough to accommodate $v_\infty^{(1)}$ and $v_\infty^{(2)}$. In other words, c_f/v_R and ρ_f/ρ are the two competitive parameters, whose interrelation decides the open arches formation. If Eq. (38) is not satisfied, then the A_0 and S_0 branches tend at $\omega \to \infty$ to the complex-valued limit, signalling that either the real locus consists of closed loop(s) or, more probably, the A_0 branch is complex throughout.

The condition $v_R < c_f < v_t$ does not affect the topology of the A and S branches, associated with the decreasing fluid modes (Eq. (12)), except that their high-frequency Scholte limit v_{Sch}, given at $c_f < v_R$ by the same relation as Eq. (37)$_2$, now shifts downwards to

$$v_{\mathrm{Sch}} = v_R\left(1 - \frac{\rho_f}{\rho}\frac{a_R}{2\sqrt{1 - v_R^2/c_f^2}}\right), \tag{39}$$

see Refs. [34,28] (the latter gave Eq. (39) with $\frac{1}{2}$ repositioned into the definition of a_R; the motivation for the present modification is made clear in Ref. [29]). The low-frequency origin of the S branch at c_f is stipulated by the condition $c_f < \hat{v}_2^{(0)}$.

Regarding the antisymmetric choice of fluid modes at $v_R < c_f < v_t$, a graphical analysis of Eq. (16) readily shows that it may also yield a real-valued arch. Denote it, say, by $\tilde{S}$. This arch conforms to the same existence considerations and, obviously, has the same high-frequency limits $v_\infty^{(1)}$ and $v_\infty^{(2)}$, as the aforementioned A_0 and S_0 arches for the choice of increasing fluid modes. It is similar in shape to the S_0 arch, but indeed has a different low-frequency 'precursor'—for a light fluid loading, the $\tilde{S}$ arch is connected by the complex-valued segment with the supersonic arch $R = 0$ of zero reflection, in agreement with the intrinsic meaning of the antisymmetric choice of fluid modes.

A numerically calculated subsonic spectrum exemplifying the case $v_R < c_f < v_t$ is presented in Fig. 8 (pure imaginary $\tilde{A}_1$ and $A_1^{(\mathrm{free})}$ branches are omitted). The choice of materials, the golden plate ($\rho = 19.3$ g/cm^3; $v_l = 3.275$, $v_t = 1.215$, $v_R = 1.148$ mm/μs) immersed into alcohol ($\rho_f = 0.8$g/cm^3, $c_f = 1.21$mm/μs), has been made for the sake of enabling a distinct graphical

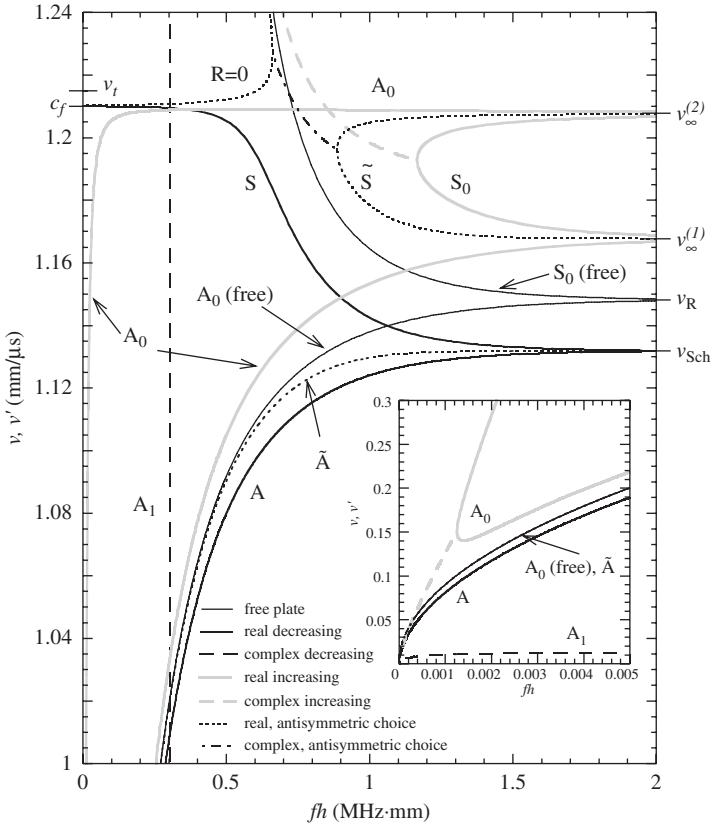

Fig. 8. The real and (real parts of) complex flexural-type branches, and the real-valued arches at various choices of the fluid modes for the golden plate in alcohol. The inset shows opening of the A_0 real arch at low frequency. The free-plate branches are added as the reference.

manifestation of the events in between c_f and v_R. Apart from the desirable relation of the velocities, this combination is characterized by markedly small ρ_f/ρ, which fulfills (38) and thus endorses the presence of the real-valued open arches. In the present case, the estimate of the lower high-frequency limit $v_\infty^{(1)}$, specified for an isotropic plate as

$$v_\infty^{(1)} = v_R\left[1 + \frac{\rho_f}{\rho}\frac{\left(v_R/v_t\right)^4}{v_R\left(\mathrm{d}f_R/\mathrm{d}v\right)_{v_R}}\sqrt{\frac{1 - v_R^2/v_l^2}{1 - v_R^2/c_f^2}}\right] \tag{40}$$

($f_R(v)$ is the Rayleigh function), yields the value which lies well below $v_\infty^{(2)} \approx c_f$. Note that Eq. (40) is in quantitative agreement with the numerical calculation [25] for the interface wave solutions in the fluid-loaded half-space of a gold–silver alloy with variable parameters, which demonstrates that the leaky-Rayleigh complex value v_{lR} transforms into two real values $v_\infty^{(1)}$ and $v_\infty^{(2)}$ once v_R becomes sufficiently less than c_f to satisfy the inequality (38). The case of the Plexiglas half-space loaded by the methanol solution with varying ρ_f and c_f [24] may be adduced as an example of the opposite situation, when the difference between v_t and v_R is too small in comparison with ρ_f/ρ to transform v_{lR} into $v_\infty^{(1)}$, $v_\infty^{(2)}$ with c_f decreasing from v_t to v_R.

5.2. The case $v_t < c_f$

Usually the velocities v_R and v_t are fairly close and so having a value of c_f in between them is a rather special setting. Considerably more common case is $v_t < c_f$. It is typical for relatively soft plate materials. However, it seems more appropriate to emphasize the 'slow' plate choice. The basic feature of this case, namely, the occurrence of infinitely repeated real-valued loops with changeover points, is a topological invariant stipulated solely by the velocity relation $v_t < c_f$, which necessitates the upper continuum of the free-plate (real) branches to slip under c_f as they tend at high ω to v_t (in the measure of $(kh)^{-2}$, see Ref. [37]).

Assuming the symmetric choice of fluid modes, let us explain the loops formation by means of the graphical display in Fig. 6d and e, which refers to the simple situation of the SH-branch uncoupling and is also scaled for not so small density ratio ρ_f/ρ in order to match the subsequent numerical example. The A_0 real arch arrives in the same fashion as before (Fig. 6d), but now, at $v_t < c_f$, it is ensured for any value of ρ_f/ρ which affects only its shape. With increasing frequency, the least zero point $\tilde{v}_1(\omega)$ of the plate-admittance curves $Y_1^{(\mathbf{n})} \pm |Y_2^{(\mathbf{n})}|$ is pushed towards v_t by the $A_1^{(\mathrm{free})}$-pole (corresponding to the first branch of the free-plate upper continuum), so this zero point meets c_f and then becomes less than c_f. As a consequence, one of the intersections of the 'plate curve' with $-Y_f$ reaches c_f and is then superseded by the intersection with Y_f (Fig. 6e). This changeover means that the ascending upper arm of the A_0 arch of real roots of Eq. (13), involving the increasing fluid modes, touches c_f and then transforms into the descending arm of real solutions of Eq. (12), involving the decreasing fluid modes (the same, in fact, occurs at $v_R < c_f < v_t$ as well, if the second Scholte interfacial solution does exist [28]). With further growing frequency, the poles of $Y_1^{(\mathbf{n})} \pm |Y_2^{(\mathbf{n})}|$, corresponding to the next free-plate branches of the upper continuum, also approach v_t and thereby entail the successive arrival of narrowing real-valued arches with a changeover point at c_f each, following with approximately the same frequency step. It is seen that, given that ω is unlimited, this infinite sequence occurs for any ρ_f/ρ, as soon as c_f is greater than v_t.

At $\omega \to \infty$, all the upper arms, associated with the decreasing fluid modes, tend to v_t. This continuum is certainly tantamount to the Sezawa family of branches in a solid substrate with 'slow' coating. The lower arms do the same, except maybe the first ones. The assessment as to which is the case can be made by checking the sign of the inequality

$$\tau \equiv \frac{Y_\infty^{(\mathbf{n})}(v_t)}{-Y_f(v_t)} \gtrless 1, \tag{41}$$

where τ is proportional to ρ_f/ρ and decreases with growing c_f. Once $\tau > 1$, the value $Y_\infty^{(\mathbf{n})}(v_t)$ lies above $-Y_f(v_t)$ and the same should be expected for the monotonically increasing curves $Y_\infty^{(\mathbf{n})}(v)$ and $-Y_f(v)$ anywhere below v_t. In this case all the lower arms tend to v_t; hence, all the arches are asymptotically closed at $\omega \to \infty$ and are most likely to be wholly bounded by v_t. The inequality $\tau < 1$ necessitates at least one intersection of $Y_\infty^{(\mathbf{n})}(v)$ and $-Y_f(v)$, which yields the high-frequency limit $v_\infty^{(1)} < v_t$ (see Eq. (37)) for the lower arms of the first two arches. Their upper arms tend to v_t, so those arches stay open at $\omega \to \infty$. The two spectral configurations, one with a single high-frequency limit v_t and the other with two limits v_t and $v_\infty^{(1)}$ ($v_R < v_\infty^{(1)} < v_t$), represent most generic patterns at the densities or/and velocities variation. Both imply that the A_0 branch does not have the leaky-Rayleigh limit v_{lR} with $v'_{lR} < v_t$, $v''_{lR} < 0$.

In principle, more elaborate situations are possible, when $\tau > 1$ or $\tau < 1$ admit, respectively, two or three intersections of $Y_\infty^{(\mathbf{n})}(v)$ and $-Y_f(v)$, thereby indicating two or three distinct high-frequency limits below v_t for the first pairs of arms. Corresponding spectral configurations enable the transitions, say, between the two above-mentioned generic patterns on continuously decreasing ρ_f/ρ, or from the pattern with two limits $v_\infty^{(1)}$, $v_\infty^{(2)}$ at $v_R < c_f < v_t$ (Fig. 8) to that with one limit $v_\infty^{(1)} < v_t$ on c_f surpassing v_t. However, these 'transitional' configurations occur in the narrow ranges of subtle relations between the densities and velocities (e.g., see Ref. [25]) and are therefore relatively unlikely to be encountered in practice. It should also be noted that introducing anisotropy breaks up the S branch and unfolds 'the former' SH branch $v_t = \text{const.}$ into two branches with the common onset at $\hat{v}_2^{(0)} < c_f$, one of them associated with the decreasing fluid modes and decreasing to v_{Sch} (instead of the former S branch) and the other one tending at $\omega \to \infty$ to the bulk-wave threshold. At the same time, these changes do not affect the two generic patterns of the looping branches, which are thus stable with respect to anisotropy perturbation as well.

In view of the recently reported results for the water-loaded Plexiglas, fulfilling the case $v_t < c_f$ [23,24,26], we consider this combination of media for a numerical example. The material parameters assumed for Plexiglas are the same as were used in Ref. [26] ($\rho = 1.18$ g/cm^3; $v_l = 2.5$, $v_t = 1.2$, $v_R = 1.12$, mm/μs).The spectrum presented in Fig. 9 complements [26] by exhibiting a sequence of real-valued arches, which swarm the subsonic spectrum with growing ω. It is instructive to note that because ρ_f/ρ is not small, the S_0 leaky wave branch with growing ω becomes fairly remote from $S_0^{(\mathrm{free})}$ and is not involved in the formation of the second arch, which, by contrast to Fig. 8, originates from another complex symmetric branch starting off from zero v and ω (but with $k = \omega/v \neq 0$, as it is seen from its linear onset, so this is not a flexural-type branch). The isotropic value

$$\tau_{\mathrm{iso}} = \frac{\rho_f}{\rho}\sqrt{\frac{1 - v_t^2/v_l^2}{1 - v_t^2/c_f^2}} \tag{42}$$

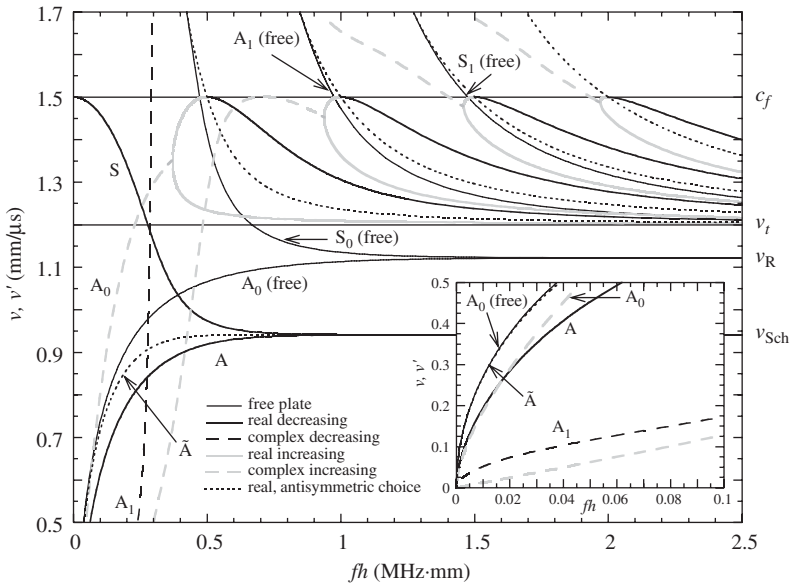

Fig. 9. The real and (real parts of) complex flexural-type branches, and the sequence of real-valued looping branches (frequency-truncated) for the Plexiglas plate in water. Also shown are the relevant fragments of the free-plate branches, the immersed-plate leaky branches and zero-reflection branches (the latter continue below c_f as real branches for the antisymmetric choice of fluid modes). The inset zooms the low-frequency onset.

in the case of Plexiglas is greater than 1, which is why all the arches lie above v_t. At the same time, e.g., for the water-loaded polyvinyl chloride (PVC), also realizing the case $v_t < c_f$, it is $\tau_{\text{iso}} < 1$ (that is, $\rho > \rho_c$ in terms of Ref. [23]), so the subsonic spectrum of the PVC plate immersed into water is to fall under the other pattern, with the lower arms of the two first arches tending to $v_\infty^{(1)} < v_t$. Note that the normal admittance of the solid half-space $Y_\infty^{(\mathbf{n})}(v)$, representing a high-frequency limit of $Y_1^{(\mathbf{n})} \pm |Y_2^{(\mathbf{n})}|$ at $v \leqslant v_t$, is constructed from the partial modes decreasing into the solid depth; therefore the fluid–solid interfacial solution mentioned in Refs. [23,25], which increases into the solid, cannot arise as a limit of the plate theory and so does not appear in the present considerations. Regarding a drastically different shape of specifically the first arch, observed in Ref. [26] for the air–Plexiglas–fluid case, it becomes evident as a general feature from graphical solution (Fig. 6f and g) of the dispersion equation for the plate loaded by a fluid on one side and free on the other, for which case the 'plate contribution' is given by $Y_1^{(\mathbf{n})}$ only.

Let us also mention the array of solutions, arising at $v_t < c_f$ for the antisymmetric choice of fluid modes. A graphical analysis of Eq. (16) reveals that its solutions complement each of the two generic patterns of the real-valued arches, related to symmetric choice, by the infinite sequence of the real curves, tending at high frequency to the same limit(s) as the arches, that is, to v_t at $\tau > 1$ or to v_t and $v_\infty^{(1)}$ at $\tau < 1$. It is significant that these curves continue into the supersonic domain, where they are the branches of zero reflection, and the points of their intersection with c_f must exactly coincide with the changeover points of the arches for the symmetric choice (see Fig. 9).

6. Conclusions

The subsonic spectrum of generally anisotropic fluid-loaded plates has been studied with two basic objectives. First, the ramification of the flexural-type family, associated with different choices of the partial mode in the fluid, has been traced by way of deriving and analysing the explicit low-frequency asymptotics derived. It is clarified that the real A and complex A_0 branches, related to the choice of either decreasing or increasing mode into the fluid depth on both sides of the plate, occur as the solutions of two different forms of the dispersion equation, not as a split of the $A_0^{(\mathrm{free})}$ branch of the free plate. Disregarding this implication is fraught with misinterpretations (see example in Section 3). Another flexural-type complex branch in the immersed-plate spectrum, the A_1 branch, evolves from the (pure imaginary) free-plate $A_1^{(\mathrm{free})}$ branch tending to the first thickness resonance. Remarkably, the A_1 branch appears only if the decreasing fluid mode is chosen. It is noted that the 'antisymmetric choice' of fluid modes—decreasing into the fluid on one side of the plate and increasing on the other—brings about two more flexural-type branches, real $\tilde{A}$ and pure imaginary $\tilde{A}_1$, which stem from $A_0^{(\mathrm{free})}$ and $A_1^{(\mathrm{free})}$, respectively. Altogether, this set of branches represents the flexural-type family for an arbitrary immersed plate. The supersonic features of the A_0 and A_1 branches are discussed, among other topics, in a companion paper [29] devoted to the spectrum of leaky waves.

The second target of the study has been the phenomenon of real-valued looping branches, associated with the choice of increasing modes in fluids. This endeavour is motivated by numerical findings for isotropic plates, broadly discussed in the literature, and also by the recent experimental observation of the looping branch for a Plexiglas plate in water [26]. A general insight into the origin and shape of the real-valued branches for any anisotropic plate can be readily gained using the graphical display of the sextic plate formalism. It visualizes the real velocity solutions $v(\omega)$ at any ω as the intersections of the fluid-admittance curve (its sign accounts for the choice of fluid modes) with the pair of plate-admittance curves, which are endowed with certain topologically invariant features. By these means, three settings leading to the essentially different subsonic spectral configurations have been envisaged. At $c_f < v_R$ and ρ_f/ρ less than the critical value $(\rho_f/\rho)_{\mathrm{crit}}$ estimated by Eq. (36a), the A_0 branch contains a closed real loop within the sector between c_f and the $A_0^{(\mathrm{free})}$ branch. If c_f lies above v_R but below the bulk-wave threshold for the plate, while ρ_f/ρ is less than a certain bound exceeding $(\rho_f/\rho)_{\mathrm{crit}}$ inasmuch as c_f exceeds v_R, then the A_0 real loop becomes an open arch and is joined by another, S_0 real arch, which appears above the $S_0^{(\mathrm{free})}$ branch after the latter slips under c_f. These two arches share the high-frequency limits $v_\infty^{(1,2)}$ of their upper and lower arms ($v_R < v_\infty^{(1,2)} < c_f$). Once c_f is greater than the bulk-wave threshold (say, v_t), the subsonic spectrum for any ρ_f/ρ contains the infinite sequence of the progressively narrowing real-valued looping branches, following one after another with approximately the same frequency step. The upper arm of each looping branch reaches c_f and undergoes a changeover into a descending curve of solutions that involve the decreasing fluid modes. Generally, either both arms of all the arches lie above v_t approaching it at $\omega \to \infty$, or else the lower arms of the two first arches are singled out by tending to $v_\infty^{(1)} < v_t$. The analytical conditions and estimates for the aforementioned patterns of the loop(s) have been derived for arbitrary anisotropic plates and then exemplified, in a more explicit form, for isotropic plates. The real-valued locus of subsonic solutions, arising at $v_R < c_f$ for the 'antisymmetric choice' of fluid modes, has also been considered and a link to the zero-reflection supersonic curves pointed out. A

clear picture of the plane-wave looping branches being in hand enables us to move on to the problem with a source, in order to explore the possible impact of those branches on the response function and assess prospects for its experimental observation.

It is noted that the basic conclusions of this paper apply, with appropriate modifications, to inhomogeneous plates with arbitrary variation of material properties across the plate, see Ref. [38].

Acknowledgements

A.L.S. acknowledges partial support from the Russian Foundation for Basic Research (grant 05-02-16666).

References

[1] A.H. Nayfeh, *Wave Propagation in Layered Anisotropic Media*, North-Holland, Amsterdam, 1995.
[2] D.E. Chimenti, Guided waves in plates and their use in material characterization, *Applied Mechanics Reviews* 50 (1997) 247–284.
[3] S.V. Sorokin, Analysis of vibrations and energy flows in sandwich plates bearing concentrated masses and spring-like inclusions in heavy fluid-loading conditions, *Journal of Sound and Vibration* 253 (2002) 485–505.
[4] A.J. Hull, D.A. Hurdis, A parameter estimation method for the flexural wave properties of a beam, *Journal of Sound and Vibration* 262 (2003) 187–197.
[5] C.H. Wang, L.R.F. Rose, Wave reflection and transmission in beams containing delamination and inhomogeneity, *Journal of Sound and Vibration* 264 (2003) 851–872.
[6] J.N. Sharma, R. Kumar, Asymptotics of wave motion in transversely isotropic plates, *Journal of Sound and Vibration* 274 (2004) 747–759.
[7] O. Poncelet, M. Deschamps, Lamb waves generated by complex harmonic inhomogeneous plane wave, *Journal of the Acoustical Society of America* 102 (1997) 292–300.
[8] A. Bernard, M. Deschamps, M.J.S. Lowe, Comparison between the dispersion curves calculated in complex frequency and the minima of the reflection coefficients for an embedded layer, *Journal of the Acoustical Society of America* 107 (2000) 793–800.
[9] O. Lenoir, J.M. Conoir, J.L. Izbicki, The complex phase gradient method applied to leaky Lamb waves, *Journal of the Acoustical Society of America* 112 (2002) 1335–1345.
[10] M.F.M. Osborne, S. D. Hart, Transmission, reflection, and guiding of an exponential pulse by a steel plate in water. I. Theory, *Journal of the Acoustical Society of America* 17 (1945) 1–18.
[11] H. Dabirikhah, C. W. Turner, Anomalous behaviour of flexural waves in very thin immersed plates, *I.E.E.E. Ultrasonics Symposium Proceedings* 1 (1992) 313–317.
[12] H. Dabirikhah, C.W. Turner, The coupling of the A_0 & interface Scholte modes in fluid-loaded plates, *Journal of the Acoustical Society of America* 100 (1996) 3442–3445.
[13] J. Dickey, G. Maidanik, H. Überall, The splitting of dispersion curves for the fluid-loaded plate, *Journal of the Acoustical Society of America* 98 (1995) 2365–2367.
[14] J.-P. Sessarego, J. Sagéloli, C. Gazanhes, H. Überall, Two Scholte-Stoneley waves on doubly fluid-loaded plates and shells, *Journal of the Acoustical Society of America* 101 (1997) 135–142.
[15] X.L. Bao, H. Franklin, P.K. Raju, H. Überall, O. Poncelet, Fluid-borne and Lamb-type waves on elastic plates in contact with two different fluids, *Acustica-Acta Acustica* 84 (1998) 823–829.
[16] A. Freedman, Anomalies of the A_0 leaky Lamb mode of a fluid-loaded elastic plate, *Journal of Sound and Vibration* 183 (1995) 719–737.

[17] J. Dickey, G. Maidanik, H. Überall, Response to Comments on 'The coupling of the A_0 & interface Scholte modes in fluid-loaded plates', *Journal of the Acoustical Society of America* 100 (1996) 3446.
[18] A.D. Stuart, Acoustic radiation from submerged plates. I. Influence of leaky wave poles, *Journal of the Acoustical Society of America* 59 (1976) 1160–1174.
[19] M. Pierucci, T.S. Graham, Unusual characteristics of free bending waves in thick plates with fluid loading, *Journal of the Acoustical Societ of America* 62 (1977) S84 (A).
[20] W.A. Strawderman, S.-H. Ko, A.H. Nuttall, The real roots of the fluid-loaded plate, *Journal of the Acoustical Society of America* 66 (1979) 579–585.
[21] C. Desmet, V. Gusev, C. Glorieux, W. Lauriks, J. Thoen, All-optical investigation of the lowest-order antisymmetrical acoustic modes in liquid-loaded membranes, *Journal of the Acoustical Society of America* 103 (1998) 618–621.
[22] A.C. Ahyi, P. Pernod, O. Gatti, V. Latard, A. Merlen, H. Überall, Experimental demonstration of the pseudo-Rayleigh (A_0) wave, *Journal of the Acoustical Society of America* 104 (1998) 2727–2732.
[23] F. Padilla, M. de Billy, G. Quentin, Theoretical and experimental studies of surface waves on solid–fluid interfaces when the value of the fluid sound velocity is located between the shear and the longitudinal ones in the solid, *Journal of the Acoustical Society of America* 106 (1999) 666–673.
[24] C. Glorieux, K. Van de Rostyne, K. Nelson, W. Gao, W. Lauriks, J. Thoen, On the character of acoustic waves at the interface between hard and soft solids and liquids, *Journal of the Acoustical Society of America* 110 (2001) 1299–1306.
[25] V.G. Mozhaev, M. Weihnacht, Subsonic leaky Rayleigh waves at liquid–solid interfaces, *Ultrasonics* 40 (2002) 927–933.
[26] K. Van de Rostyne, C. Glorieux, W. Gao, W. Lauriks, J. Thoen, Experimental investigation of leaky Lamb modes by an optically induced grating, *Transactions on Ultrasonics, Ferroelectricity and Frequency Control* 49 (2002) 1245–1253.
[27] A.L. Shuvalov, On the theory of wave propagation in anisotropic elastic plates. *Proceedings of the Royal Society London A* 456 (2000) 2197–2222.
[28] A.L. Shuvalov, Theory of plane subsonic elastic waves in fluid-loaded anisotropic plates, *Proceedings of the Royal Society London A* 458 (2002) 1323–1352. (Note the misprints in (2.8): $\mathbf{Y}_2 = \mathrm{i}\mathbf{M}_3^{-1}$ (same in Ref. [27]), in Fig. 3a,b: the zeros must be denoted by $\tilde{v}_j$ (not $\hat{v}_j$), and on the last but one line of p. 1332: the reference is to Section 2*f* (not 2*c*)).
[29] A.L. Shuvalov, O. Poncelet, M. Deschamps, Analysis of the dispersion spectrum of fluid-loaded anisotropic plates: leaky wave branches, *Journal of Sound and Vibration,* accepted for publication.
[30] A.N. Stroh, Steady state problems in anisotropic elasticity, *Journal of Mathematics and Physics* 41 (1962) 77–103.
[31] J. Lothe, D.M. Barnett, On the existence of surface-wave solutions for anisotropic half-spaces with free surface, *Journal of Applied Physics* 47 (1976) 428–433.
[32] P. Chadwick, G.D. Smith, Foundations of the theory of surface waves in anisotropic elastic materials, *Advances in Applied Mechanics* 17 (1977) 303–376.
[33] T.C.T. Ting, *Anisotropic Elasticity*, Oxford University Press, Oxford, 1996.
[34] D.M. Barnett, S. D. Gavazza, J. Lothe, Slip waves along the interface between two anisotropic elastic half-spaces in sliding contact, *Proceedings of the Royal Society London A*. 415 (1988) 389-419
[35] X.L. Bao, H. Franklin, P.K. Raju, H. Überall, Fluid-borne and Lamb-type waves on elastic plates in contact with two different fluids, *Journal of the Acoustical Society of America* 102 (1997) 1246–1248.
[36] L. Wang, J. Lothe, Existence of second slip waves in anisotropic elastic media, *Wave Motion* 18 (1993) 79–99.
[37] V.I. Alshits, M. Deschamps, G.A. Maugin, Elastic waves in anisotropic plates: short-wavelength asymptotics of the dispersion branches $v_n(k)$, *Wave Motion* 37 (2003) 273–292.
[38] A.L. Shuvalov, O. Poncelet, M. Deschamps, General formalism for plane guided waves in transversely inhomogeneous anisotropic plates, *Wave Motion* 40 (2004) 413–426
A.L. Shuvalov, O. Poncelet, C. Baron, M. Deschamps, Long-wavelength dispersion of acoustic waves in transversely inhomogeneous anisotropic plates, *Wave Motion* 42 (2005) 367–382.